

Inner magnetospheric heavy ion composition during high-speed stream-driven storms

D. R. Forster,¹ M. H. Denton,^{1,2} M. Grande,³ and C. H. Perry⁴

Received 21 December 2012; revised 2 April 2013; accepted 22 April 2013; published 1 July 2013.

[1] Ion composition data, taken by the Combined Release and Radiation Effects Satellite Magnetospheric Ion Composition Spectrometer instrument, are investigated across eight high-speed solar wind-stream-driven storms (HSSs) during 1991. The HSSs are identified using solar wind data from OMNI alongside geomagnetic indices, and the behavior of ions in the energy range 31.2–426.0 keV is investigated. A case study of the single HSS event that occurred on 30 July 1991 is performed, and superposed epoch analyses of five events are conducted. The data show evidence of a local minimum (dropout) in the flux and partial number density of ionic species H^+ , He^+ , He^{++} , and O^+ close to the onset of magnetospheric convection. The flux and number density rapidly fall and then recover over a period of hours. The initial rapid recovery in number density is observed to consist primarily of lower-energy ions. As the number density reaches its maximum, the ions show evidence of energization. Heavy ion-to-proton ratios are observed to decrease substantially during these HSS events.

Citation: Forster, D. R., M. H. Denton, M. Grande, and C. H. Perry (2013), Inner magnetospheric heavy ion composition during high-speed stream-driven storms, *J. Geophys. Res. Space Physics*, 118, 4066–4079, doi:10.1002/jgra.50292.

1. Introduction

[2] Geomagnetic storms due to high-speed solar wind streams (HSS) occur most regularly during the declining phase of the solar cycle [e.g., *Tsurutani et al.*, 2006, and references therein; *Borovsky and Denton*, 2009a] due to the extension of solar coronal holes toward the solar equator. Coronal holes emit fast solar wind ($\sim 500\text{--}800\text{ km s}^{-1}$), while the ambient solar wind is much slower ($\sim 300\text{--}400\text{ km s}^{-1}$). The fast wind and the slow wind interact leading to elevated density and pressure. The fast solar wind which follows the interaction region typically persists for several days. These structures are known as Corotating Interaction Regions (CIRs), their highly repeatable nature means that the technique of superposed epoch analysis is particularly applicable to their study. Such structures in the solar wind are known to stimulate repeatable activity in the thermosphere [e.g., *Turunen et al.*, 2009; *Mlynczak et al.*, 2010], ionosphere [e.g., *Denton et al.*, 2009a; *McPherron et al.*, 2009; *Pokhotelov et al.*, 2010], plasma sheet [e.g., *Denton and Borovsky*, 2009], ring current [e.g., *Liemohn et al.*, 2006; *Jordanova et al.*, 2009], both in terms of particle and wave phenomena [e.g., *Sandanger et al.*, 2009; *MacDonald et al.*, 2010; *Posch et al.*, 2010].

[3] The timeline of magnetospheric events which occur during the passage of a HSS has been tabulated by *Borovsky*

and *Denton* [2009a]. Following arrival at Earth's magnetosphere, the fast solar wind drives strong magnetospheric convection and geomagnetic activity. Coronal holes corotate with the Sun and can last for several rotations, leading to repeatable structures of slow-then-fast solar wind which subsequently impact the Earth with approximately 27 day periodicity.

[4] Very little work has been carried out with regard to HSS storms during the time of the Combined Release and Radiation Effects Satellite (CRRES) mission, due both to the fact that CRRES was operational at solar maximum and due to the lack of continuous solar wind data, which makes HSS-identification difficult. Solar wind measurements during 1991 were taken by the Earth-orbiting Interplanetary Monitoring Platform-8 satellite, which spent between 4.5 and 5.5 days of each 12.5 day orbit within the magnetospheric cavity. During these periods, it could record no solar wind data. *Lam et al.* [2009] carried out a comparison between in situ and modeled electron observations for a pair of separate CIRs between July and September 1991. The Radial Diffusion Combined with Atmospheric Loss (RADICAL) model, described in *Lam et al.* [2007], was used to show that modeled data could adequately describe in situ observations at $L=5.0 R_E$ but was less successful at lower L shells. RADICAL had been previously shown to model the electron radiation belts with good accuracy in *Lam et al.* [2007] over 150 days in 1991, a period dominated by coronal mass ejection (CME)-driven storms.

[5] A survey of the literature reveals no indication that a dropout of the ions during HSS-driven storms has been investigated previously. By “dropout,” we specifically mean a sudden local minima in the measured energetic ion flux and/or density concurrent with the arrival of a HSS. For the well-known electron dropout, the flux is typically observed to decrease between 1 and 5 orders of magnitude. The dropout in electrons that occurs in the Earth's outer radiation belt during HSS-driven storms is a well-known phenomenon [e.g., *Tsurutani et al.*, 2006; *O'Brien*

Additional supporting information may be found in the online version of this article.

¹Department of Physics, Lancaster University, Lancaster, UK.

²Space Science Institute, Boulder, Colorado, USA.

³Institute of Mathematics and Physics, Aberystwyth University, Aberystwyth, UK.

⁴Rutherford Appleton Laboratory, Didcot, UK.

Corresponding author: D. R. Forster, Department of Physics, Lancaster University, Lancaster LA1 4YB, UK. (d.forster@lancaster.ac.uk)

Table 1. HSS Events During 1991

Event Date (1991)	Onset Time (UT)	Clear Solar Wind Data?	Included in Epoch Analysis?
23 January	00:00	Yes	Yes
18 February	20:00	Yes	Yes
20 May	01:00	Yes	Yes
14 July	16:00	No	No
30 July	16:00	Yes	Yes
12 August	13:00	No	No
28 August	15:00	Yes	No
7 September	00:00	Yes	Yes

Shown are the date/time of the event, whether the HSS is clear in solar wind data and a note on inclusion in subsequent superposed epoch analyses. Inclusion in the superposed epoch analysis is dependent on the D_{ST} signature; events with intense storm signatures near the onset were rejected. Onset time defines the onset of magnetospheric convection, as noted by a sharp rise in K_p index.

et al., 2001; Borovsky and Denton, 2009a and references therein]. There are several effects that may contribute to the dropout, involving processes which lead to either atmospheric or outer magnetospheric loss [e.g., Green *et al.*, 2004]. The primary effects are generally believed to be (1) pitch angle scattering due to wave-particle interactions [e.g., Horne and Thorne, 2000, 2003; Meredith *et al.*, 2002; Summers and Thorne, 2003; Rodger *et al.*, 2008; Borovsky and Denton, 2009a; Fraser *et al.*, 2010; Meredith *et al.*, 2011]; (2) inward or outward transport processes [e.g., Kim and Chan, 1997; Reeves *et al.*, 1998; Millan and Thorne, 2007; Kim *et al.*, 2010]; and/or (3) losses due to magnetopause shadowing [e.g., Shprits and Thorne, 2004; Shprits *et al.*, 2006; Ukhorskiy *et al.*, 2006], which involves a loss of particles through the dayside magnetopause as a result of its inward motion due to enhanced solar wind dynamic pressure.

[6] It is assumed that pitch angle scattering leads to loss of electrons to the atmosphere (M. A. Clilverd *et al.*, Energetic electron precipitation characteristics observed from Antarctica during a flux dropout event, submitted to *J. Geophys. Res.*, 2013) which could be somewhat modulated by changes in the heavy ion composition of the ring current due to their effect on Electromagnetic Ion Cyclotron (EMIC) wave activity [e.g., Meredith *et al.*, 2003; Summers and Thorne, 2003; Thorne *et al.*, 2006; Summers *et al.*, 2007]. EMIC waves are left-hand polarized, transverse waves which arise due to the proton cyclotron instability, and the heavy ion population of the ring current is known to act as a catalyst toward their generation and propagation [e.g., Gomberoff and Neira, 1983; Kozyra *et al.*, 1984]. In addition, equatorial magnetosonic waves (also known as Bernstein waves), [Horne and Thorne, 1998; Horne *et al.*, 2000] have been suggested as a possible mechanism for electron acceleration, when the energetic ion distribution exhibits a possible slope. Recent work has demonstrated the variability of such distributions during HSS-driven storms [Thomsen *et al.*, 2011]. The knowledge of ion behavior during enhanced geomagnetic activity is critical for understanding the physics involved in coincident electron dynamics. The relative contribution of established energization and loss processes for electrons during HSS events is the subject of energetic debate within the community. The aim of this current paper is to outline the behavior of ions in the ring current during HSS events and compare and contrast to the established electron morphology by examining the ion behavior in the outer radiation belt during HSSs—a subject that has been somewhat overlooked in recent years.

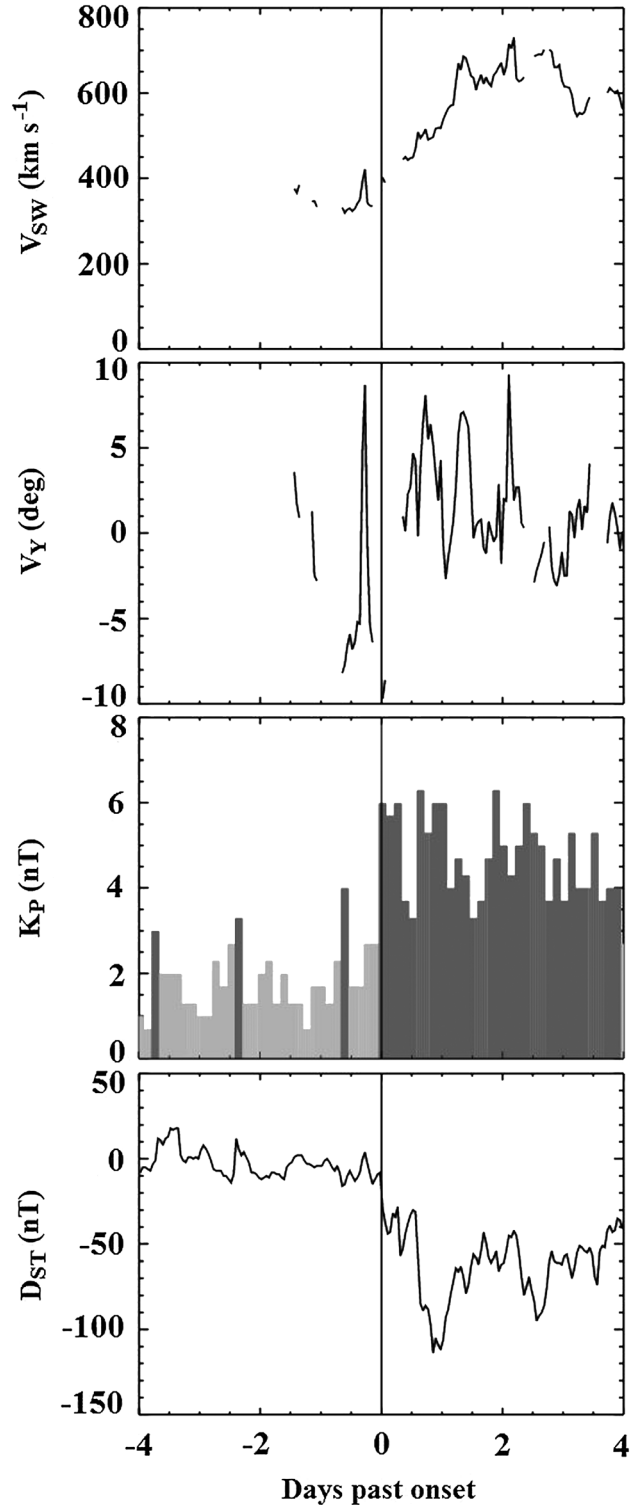


Figure 1. (top) Plots of v_{SW} , (upper middle) v_Y , (lower middle) K_p , and (bottom) D_{ST} across an HSS event from 30 July 1991. At zero, v_{SW} is observed to increase, v_Y shears, K_p is enhanced, and D_{ST} dips. A “calm before the storm” is also evident in the K_p index, noted to be a regular feature of HSS-driven storms [Borovsky and Steinberg, 2006; Clilverd *et al.*, 1993].

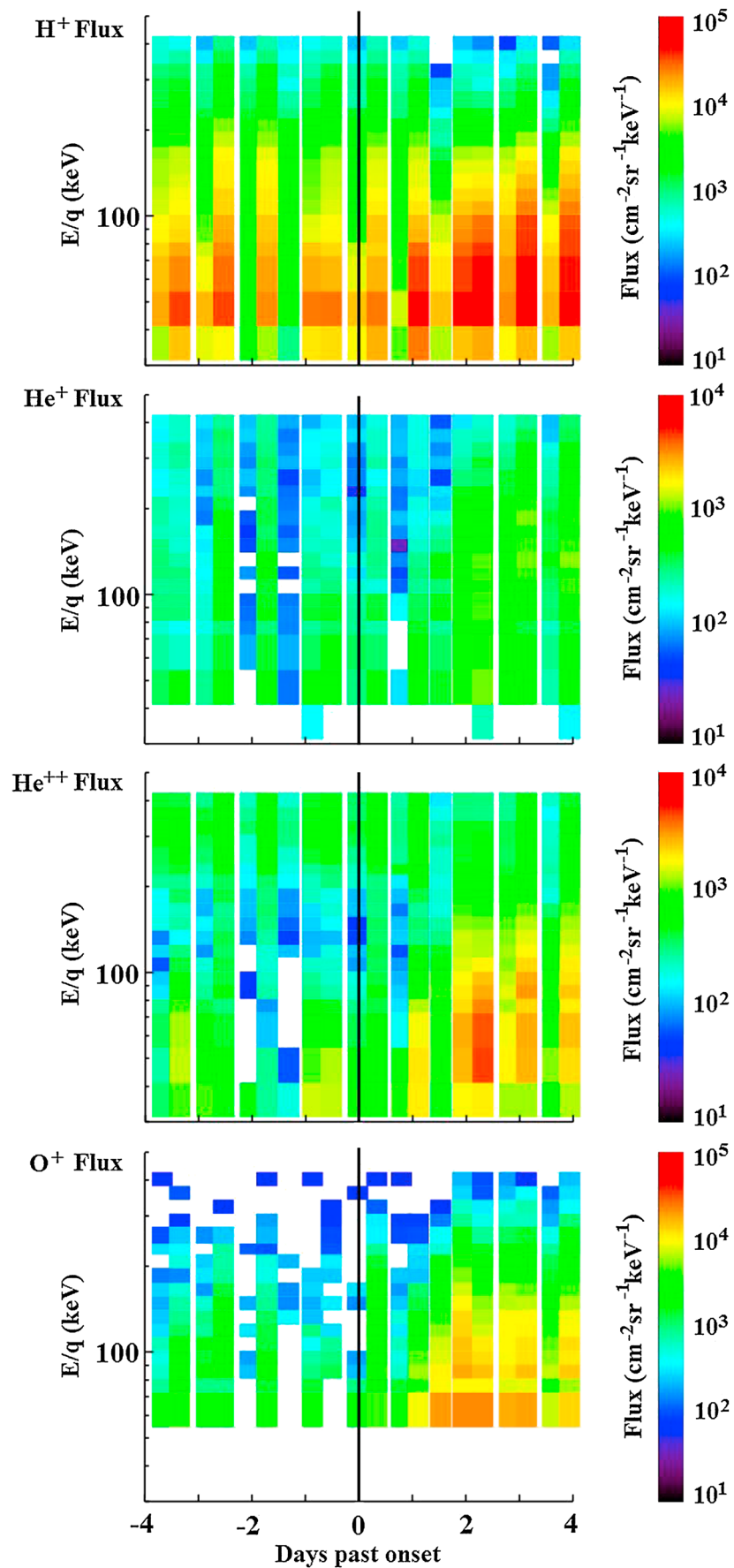


Figure 2

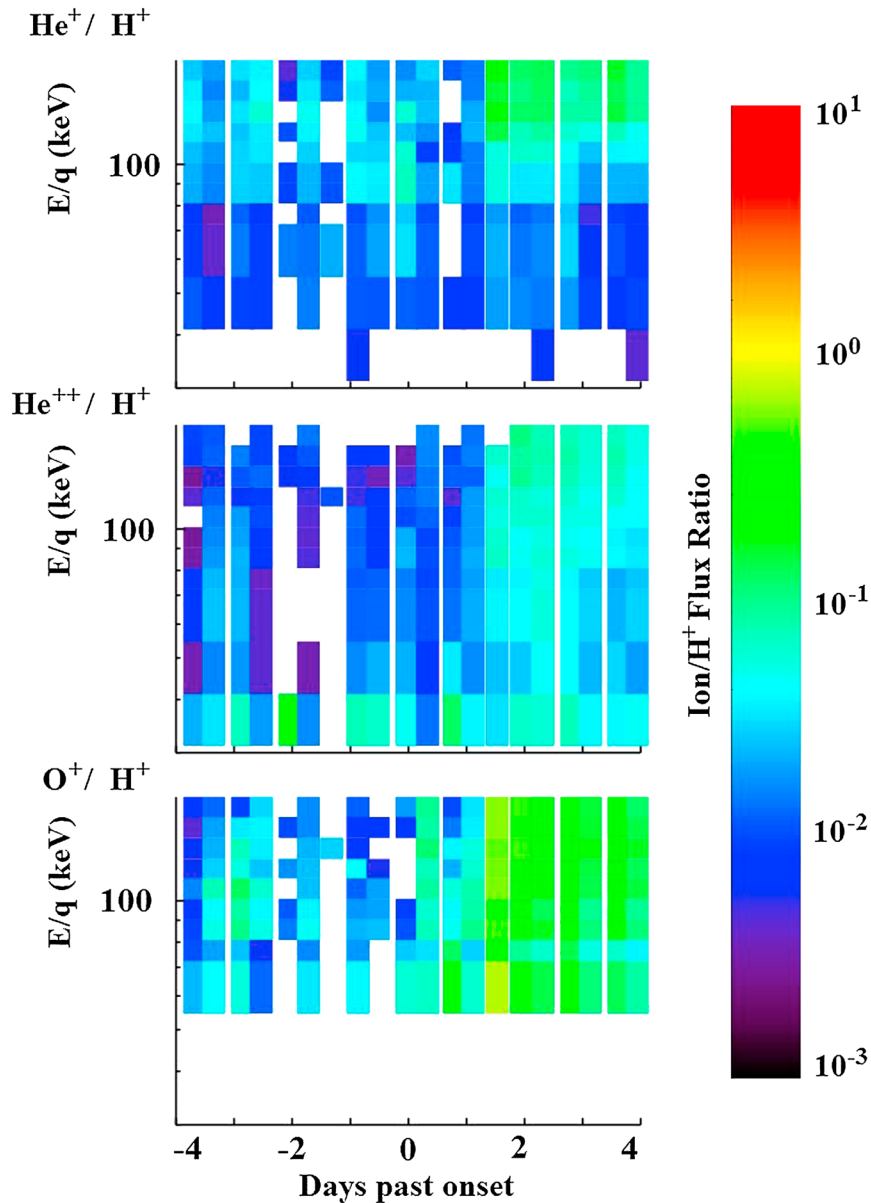


Figure 3. Average heavy ion to H^+ flux ratios between L shells of $4.0 R_E$ and $7.0 R_E$, showing (top) He^+/H^+ , (middle) He^{++}/H^+ , (bottom) and O^+/H^+ . The heavy ion content of the ring current is observed to greatly increase following an HSS event. He^+ and He^{++} flux show an increase relative to H^+ approximately 36 h following the onset of convection. O^+ flux shows a more immediate increase relative to H^+ , and after 36 h, the O^+/H^+ ratio has moved in favour of O^+ , with the two species existing in near-equal quantities.

[7] In this paper, data from the Magnetospheric Ion Composition Spectrometer (MICS) onboard CRRES are investigated for five examples of HSS-driven storms during 1991. Section 2 contains a discussion of the data sets used in the investigation and a summary of the procedure used to identify HSS events. Section 3 contains a case study of the HSS event that occurred on 30 July 1991 [labelled CIR 2 in *Lam et al., 2009*] and a superposed epoch analysis of CRRES/MICS ion flux and partial number density data from the five events that

were identified during 1991. Section 4 contains a discussion of the results, and Section 5 summarizes our conclusions.

2. Data Sets and HSS Identification

[8] In this section, the data and instrumentation used in the study will be discussed, alongside details regarding the method of determination of HSS periods from solar wind data and geomagnetic indices.

Figure 2. Energy-per-charge spectrograms for the event on 30 July 1991, showing data for (top) H^+ , (upper middle) He^+ , (lower middle) He^{++} , (bottom) and O^+ , between L shells of $4.0 R_E$ and $7.0 R_E$. The total flux is averaged for each energy range for every CRRES orbit, within the L range of $4 R_E$ to $7 R_E$. A moderate flux dropout is evident prior to zero, most notably in species He^{++} and O^+ . Following zero, there is a notable increase in the flux of all species.

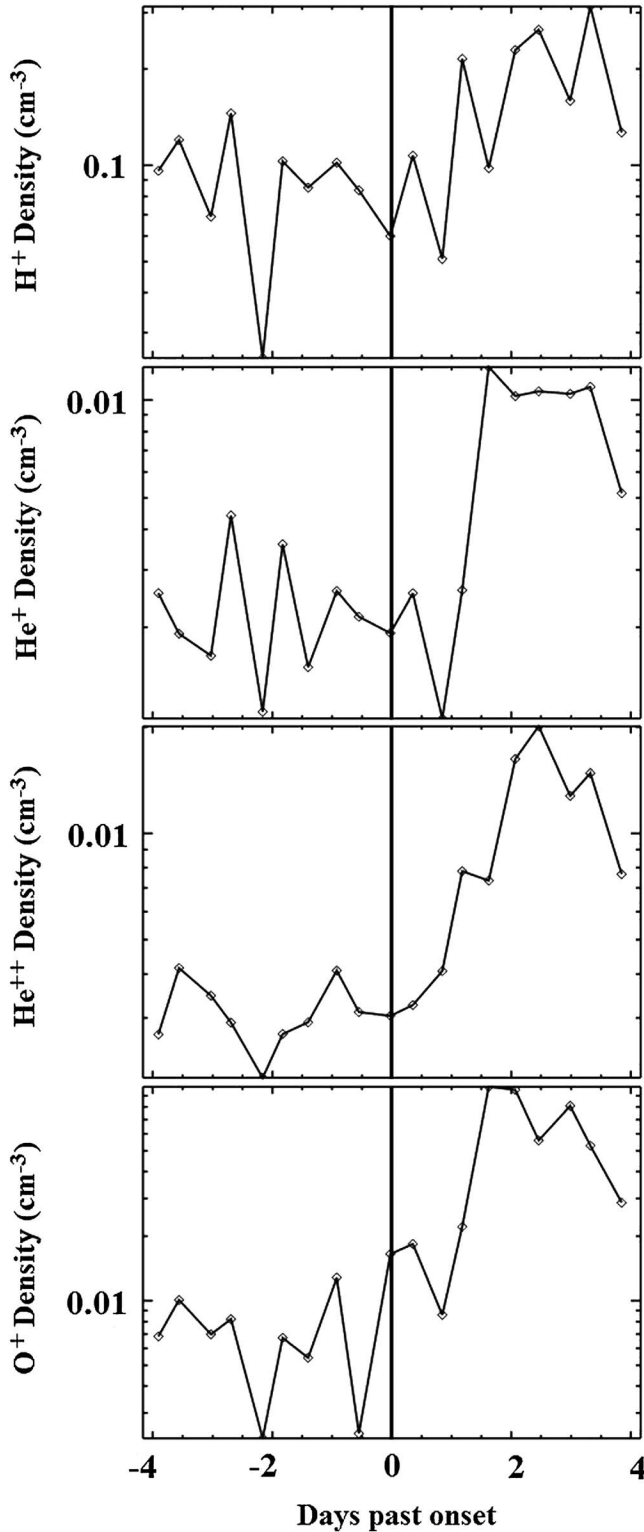


Figure 4. Ion partial number density for the event on 30 July 1991, showing data for (top) H^+ , (upper middle) He^+ , (lower middle) He^{++} , (bottom) and O^+ between L shells of $4.0 R_E$ and $7.0 R_E$. O^+ number density was calculated above 54.6 keV due to there being no data below that point. The y axis shows the average partial number density calculated for each orbit of CRRES. Following the onset of convection, there is a notable increase in the partial number density of all species.

2.1. The CRRES Mission

[9] CRRES, a joint NASA and U. S. Air Force mission, was launched on 25 July 1990 into a geostationary transfer orbit with a perigee of $\sim 1.1 R_E$ and an apogee which ranged between $\sim 6.0 R_E$ and $\sim 8.0 R_E$ through the mission. CRRES's orbital period was ~ 10 h. The magnetic local time (MLT) position of the apogee ranged from $\sim 08:00$ MLT at the beginning of the mission to $14:00$ MLT at the end. The CRRES orbit was near-equatorial with an inclination of 18.1° . The spin axis of the spacecraft was in the YZ_{GSE} plane with a rotation period of 27 s, allowing instruments to measure a full range of pitch angles. Due to the onboard battery failure, the planned 3 year mission lasted only 13 months, but during this time, the MICS instrument collected valuable data from the entire inner magnetosphere.

2.2. The MICS Instrument

[10] The MICS instrument was able to fully characterize ion species from hydrogen to iron within the energy range 31.2 – 426.0 keV. Full characterization yielded measurements of mass, charge, velocity, and hence the identity and energy of the particles. MICS utilized time-of-flight (T) and energy (E) measurements, and an E/q filter was used to identify the ionic charge. For a complete description of the operation of the CRRES MICS device, see Wilken *et al.* [1992].

[11] For this current study, the fluxes of separate ion species were averaged for individual energy bins during each 10 h orbit, between L shells of $4.0 R_E$ and $7.0 R_E$, encompassing the ring current/outer radiation belt region. Given the time scale of electron dropouts, 10 h binned data are deemed adequate for this study. We do not consider composition changes due to the changes in MLT around the CRRES orbit.

2.3. Locating HSSs During the CRRES Mission

[12] At the leading edge of a CIR, the compressed slow and fast wind leads to an enhancement in density (ρ) and pressure (P), observed in the satellite data as a peak in both parameters. The y component of solar wind velocity (v_y) within the CIR indicates a characteristic east-west deflection due to the interaction between the fast and slow wind. An increase in solar wind velocity (v_{sw}) follows the CIR and typically lasts for several days.

[13] The main issue in identifying CIRs/HSSs in the CRRES era is due to the sparsity of solar wind data. Despite this shortcoming, identification of HSSs is not impossible. In addition to the solar wind signatures of a CIR and the following HSS, repeatable signatures in geomagnetic indices can also be used to help identify and locate HSSs. The K_p index, a proxy for global magnetospheric activity [Thomsen, 2004], shows a rapid enhancement which is often preceded by a period of calm [e.g., Clilverd *et al.*, 1993; Borovsky and Steinberg, 2006; Borovsky and Denton, 2009b]. The D_{ST} index typically displays a shallow minimum during an HSS-driven storm, the relatively low magnitude of which indicates a much less intense ring current than that during a typical CME-driven storm. On occasion, the low-intensity D_{ST} signature of some HSS-driven storms has caused them to be overlooked in storm studies; an omission which has been referred to as the “ D_{ST} mistake” [Denton *et al.*, 2009b].

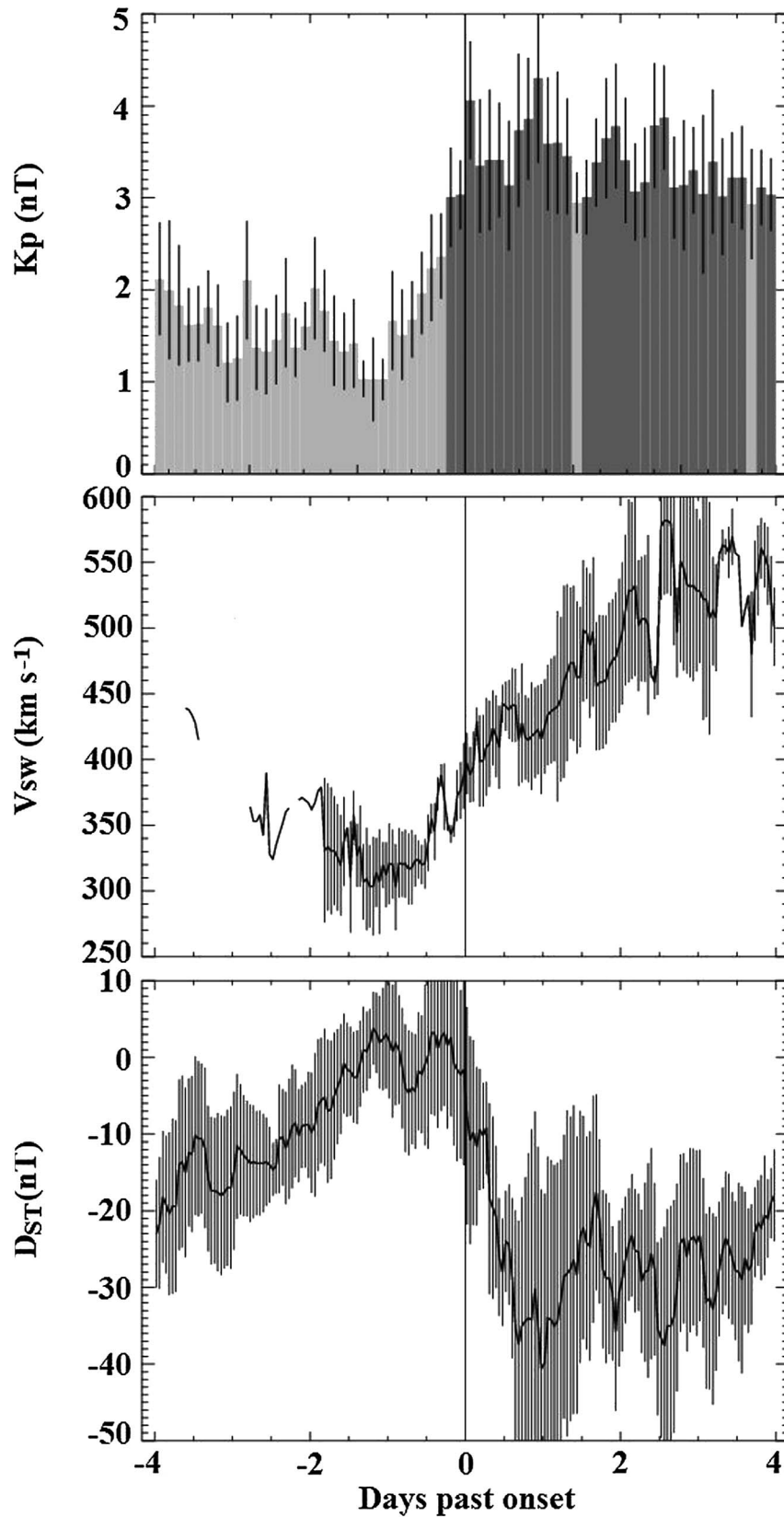


Figure 5. Graphs showing average (top) K_p , (middle) v_{sw} , and (bottom) D_{ST} for the superposed epoch analysis. Error bars show the standard error on the mean value for K_p and D_{ST} . Onset time was selected as the sharp increase in K_p associated with the onset of convection.

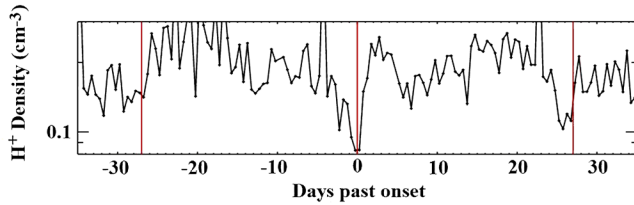


Figure 6. Superposed epoch analysis, showing H^+ partial number density across ± 35 days. The red vertical lines indicate the zero epoch and ± 27 day periods, marking approximate solar rotations. Recurrent dropouts in partial number density are observed, supporting the events as CIRs.

[14] In order to locate HSS events during the period when MICS was operational, solar wind parameters of ρ , P , v_y , and v_{sw} are examined where available. Due to the lack of solar wind data, the geomagnetic indices D_{ST} and K_p are also examined to help confirm the presence of HSS signatures. To maximize the number of events in this study, the solar wind data 27 days before and after confirmed HSSs are examined to investigate whether clear HSS signatures are visible (as may be expected for corotating structures). Using this method, a total of eight HSS events are identified during 1991, their details are given in Table 1 (see also Figure 6).

[15] The zero epoch for superposed epoch analysis is determined using K_p and is defined as the point when the index undergoes an increase of at least one full value (e.g., from 1+ to 2+), following an initial calm period. The zero epoch is thus a proxy for the onset of magnetospheric convection due to the HSS [Borovsky and Denton, 2006; Denton and Borovsky, 2008] with the choice of zero epoch being critical for superposed epoch studies [Ilie et al., 2008].

3. Results

[16] The results of the investigation will be presented over two sections, section 3.1 presents the event from 30 July 1991 as a case study, and section 3.2 presents the superposed epoch analysis of all five events.

3.1. Case Study, 30 July 1991

[17] Figure 1 contains plots of solar wind parameters v_{sw} (top) and v_Y (upper middle), as well as geomagnetic indices K_p (lower middle) and D_{ST} (bottom), for the HSS event of 30 July, 1991. Solar wind data are taken from the OMNI database [King and Papitashvili, 2005]. During 1991, solar wind data were limited. Despite this, the signature of the onset of a HSS is clearly observed in v_{sw} as a relatively steady transition from low to high speed. There is also evidence of a shear in v_Y , noted to be a feature of the interaction region ahead of the HSS. HSS-like signatures are also observed in the geomagnetic indices K_p and D_{ST} , showing a clear period of calm K_p followed by a sharp increase at onset and a fall in D_{ST} due to the enhanced ring current associated with the storm. The evolution of solar wind parameters and geomagnetic indices during this event corresponds well to typical signatures of HSS events noted by other authors [e.g., Tsurutani et al., 2006; Borovsky and Denton, 2009a]. Given the lack of complete solar wind coverage for our events, we estimate a possible error of ± 6 h in the determination of the zero epoch for all the events in this study.

[18] Figure 2 contains energy-per-charge spectrograms for H^+ (top), He^+ (upper middle), He^{++} (lower middle), and O^+ (bottom) during the event of 30 July 1991. For each spectrogram, the measured fluxes between L shells of $4.0 R_E$ and $7.0 R_E$ are averaged over an orbit. A moderate depletion of flux is observed prior to onset. This fall is clear in He^{++} data, where the flux drops by an approximate factor of 5, and O^+ and He^+ data, where the flux falls by approximately an order of magnitude. In H^+ data, there is less evidence of a fall in flux. Where clear, the “dropout” ends very soon after onset, when the flux of all ion species is observed to increase. The recovery of ion flux commences at low energies initially and then extends to higher energies during the extended period of fast solar wind. The flux enhancement occurs at the same time as the D_{ST} trough observed in Figure 1, indicating the growth of an enhanced ring current at this time.

[19] Figure 3 contains spectrograms of ion-to- H^+ flux ratios for He^+ (top), He^{++} (middle), and O^+ (bottom). Instrumental noise was clear in the data for this figure and was removed prior to calculation of the ratio. The y axis shows energy-per-charge, the x axis time, and the color indicates the value of the flux ratio, as shown in the color bar on the right. Prior to onset, H^+ exists in greater amounts than all other species: dominating over He^+ and He^{++} with a flux ratio of $\sim 10^{-2}$. During the same pre-onset period, O^+ is also present in lesser amounts than H^+ , with the ratio being between 10^{-2} and 10^{-1} . Following onset, there is an increase in heavy ion flux. In O^+ , this happens immediately, with the ratio shifting to $\sim 10^{-1}$. After ~ 30 h, He^{++} and O^+ ratios increase by around an order of magnitude, with He^{++}/H^+ reaching a value of 10^{-2} and O^+/H^+ reaching approximate unity. During the same period, He^+/H^+ increases to $\sim 10^{-1}$ above ~ 100 keV but stays at pre-onset values below this energy. In summary, the heavy-ion-to- H^+ ratio is low during the dropout phase and dramatically increases following the onset of convection and remains elevated during this HSS-driven storm.

[20] Figure 4 contains plots of the partial number density of H^+ (top), He^+ (upper middle), He^{++} (lower middle), and O^+ (bottom) ions during this event. The number density of O^+ ions could only be calculated using ions above energy 54.6 keV as O^+ ions below this energy could not penetrate the surface barrier of the solid state detector. Hence, all “density” measurements discussed below are more correctly “partial densities.” However, examination of the partial number density of electrons in the outer radiation belt and magnetotail, as opposed to simply observing the flux, have previously provided an alternative view of the dropout phenomena, and subsequent recovery [Cayton et al., 1989; Denton et al., 2010; Borovsky and Cayton, 2011; Denton and Cayton, 2011; D. P. Hartley et al., Case studies of dropouts in the electron radiation belt: Flux, magnetic field, and phase space density, submitted to *J. Geophys. Res.*, 2013]. Within Figure 4, each point corresponds to the average partial number density observed by CRRES between L shells of $4.0 R_E$ and $7.0 R_E$ during each orbit. A shallow dropout appears to occur around 80 h before the defined convection onset time. Following zero epoch (the onset of convection), a clear increase is observed in the partial number density of all species. The partial density of each ion increases substantially: O^+ , He^+ , and He^{++} densities increase by approximately a full order of magnitude, though H^+ only increases by a factor of ~ 2 . The relatively large increase in heavy ion content would cause a positive shift in the heavy-ion-to- H^+

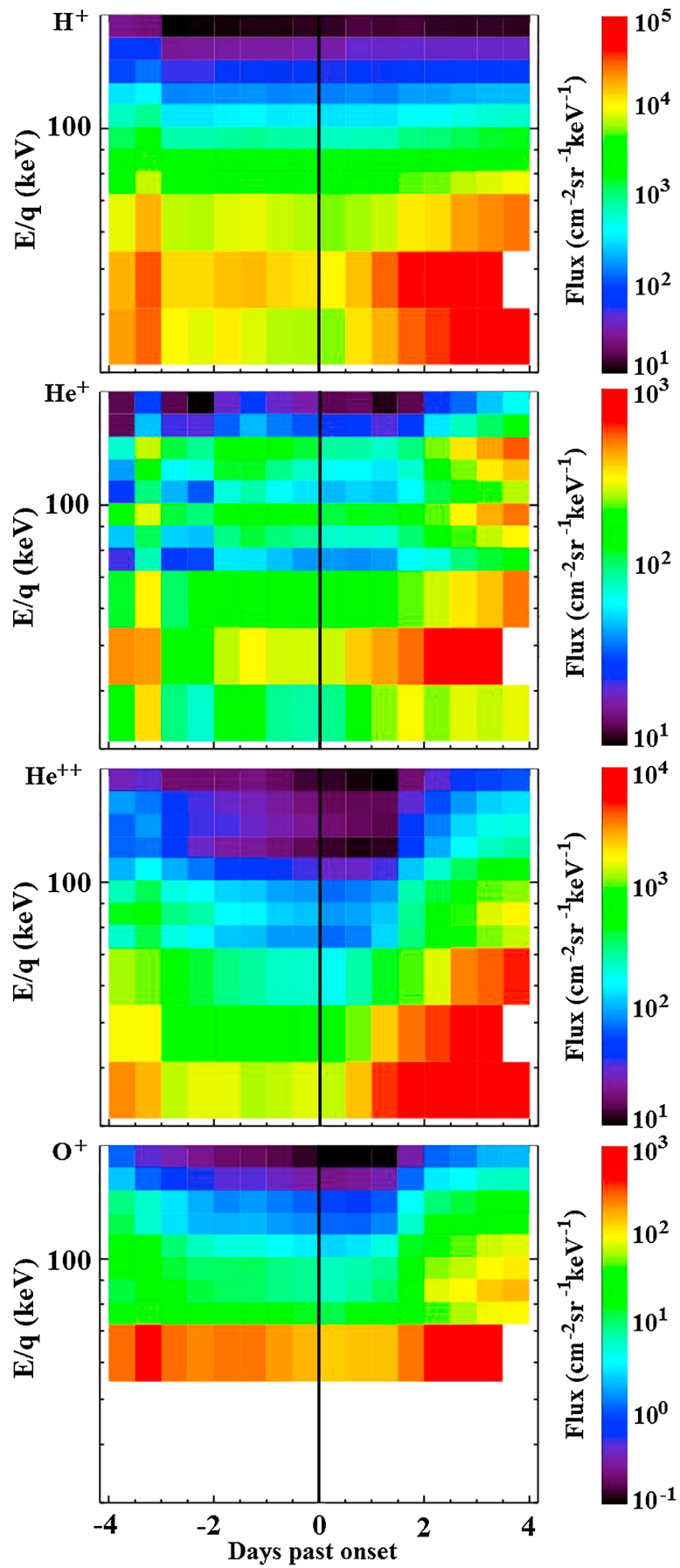


Figure 7

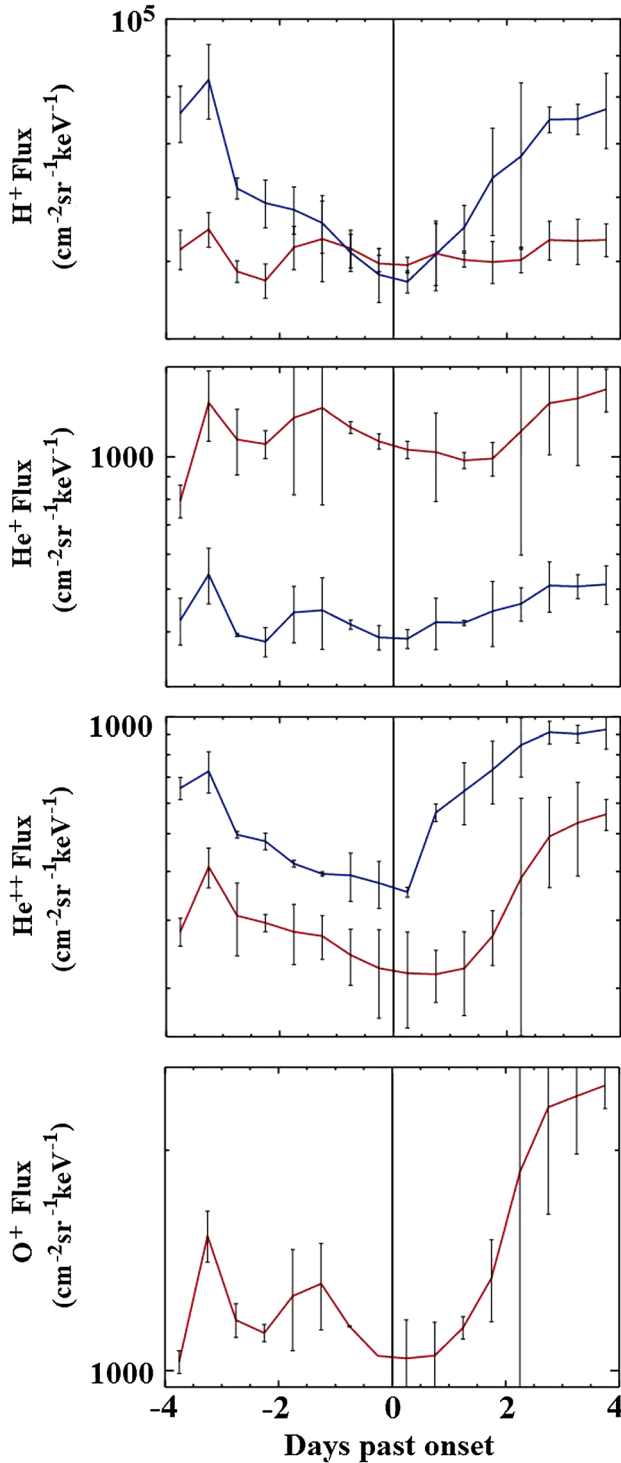


Figure 8. Superposed epoch analysis of five HSS events from 1991, showing average flux in energy ranges (blue) 31.2–54.6 keV and (red) 81.0–175.0 keV for (top) H^+ , (upper middle) He^+ , (lower middle) He^{++} , (bottom) and O^+ . A dropout is clearly visible across zero for all species within both ranges, though very little occurs in high-energy H^+ . O^+ data were not available in the lower energy range. Error bars show the standard error on the mean value of each bin.

Figure 7. Superposed epoch analysis of five HSS events from 1991, showing E/q orbit-averaged flux against epoch time for (top) H^+ , (upper middle) He^+ , (lower middle) He^{++} , (bottom) and O^+ . In these spectra, evidence of a dropout is notable across zero in all species.

ratio after onset. This increase in partial density of all ion species correlates well with the observed reduction in D_{ST} in Figure 1 and the flux enhancement in Figure 2.

3.2. Superposed Epoch Analysis

[21] A superposed epoch analysis of partial number density and particle flux was carried out for ionic species H^+ , He^+ , He^{++} , and O^+ using CRRES MICS data from the five HSS events during 1991 noted in Table 1. These were the only “clean” HSS events positively identified during the CRRES era. Three further events were found to contain very high levels of geomagnetic activity prior to onset (they contained D_{ST} signatures which were large compared with those of the events themselves), which may indicate the presence of ejecta; hence, these events were not included in the subsequent analyses. Data from the five chosen events were averaged by orbit and then sorted into 12 h time bins. General features notable in each individual event are enhanced by their superposition and are outlined below.

[22] Figure 5 contains graphs of v_{SW} (middle) and the averaged geomagnetic indices K_p (top) and D_{ST} (bottom) from the five HSS events identified in Table 1. Error bars show the standard error on the mean value for the geomagnetic indices. Similar features can be seen in each event though the magnitudes of these features vary substantially. All five events contain clear HSS signatures at onset: a steady increase in v_{SW} due to the HSS arrival, a shear in v_Y due to east-west deflection, a relatively calm period of K_p followed by a sharp increase as a result of convection, and a reduction in D_{ST} due to the weakly enhanced ring current associated with these events.

[23] Figure 6 contains the results of the superposed epoch analysis of H^+ data in all five events over the duration of ± 35 days. Such extended duration analysis is useful to confirm that corotating features are being analyzed [cf. Denton *et al.*, 2010, Figure 6]. Twenty-seven days before and after zero epoch are marked by red lines on the graphs in order to indicate the approximate duration of a solar rotation. For all species, clear dropouts in partial number density occur both 27 days before and 27 days after the zero epoch, providing evidence that the events are indeed associated with recurrent solar wind features and strongly supporting their identity as CIRs/HSSs. Following the ion dropouts, all species generally increase in partial number density, this being clearest in the CIRs that impact the Earth one solar rotation before the defined onset time.

[24] Figure 7 contains the results of the superposed epoch analysis of ion flux data in the energy range 31.2–175.0 keV for H^+ (top), He^+ (upper middle), He^{++} (lower middle), and O^+ (bottom). O^+ is shown above 54.6 keV as below this range, it could not penetrate the solid state detector, and hence there was no data. Energies above 175.0 keV are not shown in order to provide greater resolution within the lower energy range. A dropout is observed in all species, occurring most clearly in H^+ , He^{++} , and O^+ , very close to the onset of convection. The dropout occurs across this entire energy range (and at the higher energies). At the time of maximum dropout, the flux in each energy range is reduced by approximately half an order of magnitude. The exception to this is He^+ , which displays a less clear dropout. The recovery in flux begins immediately

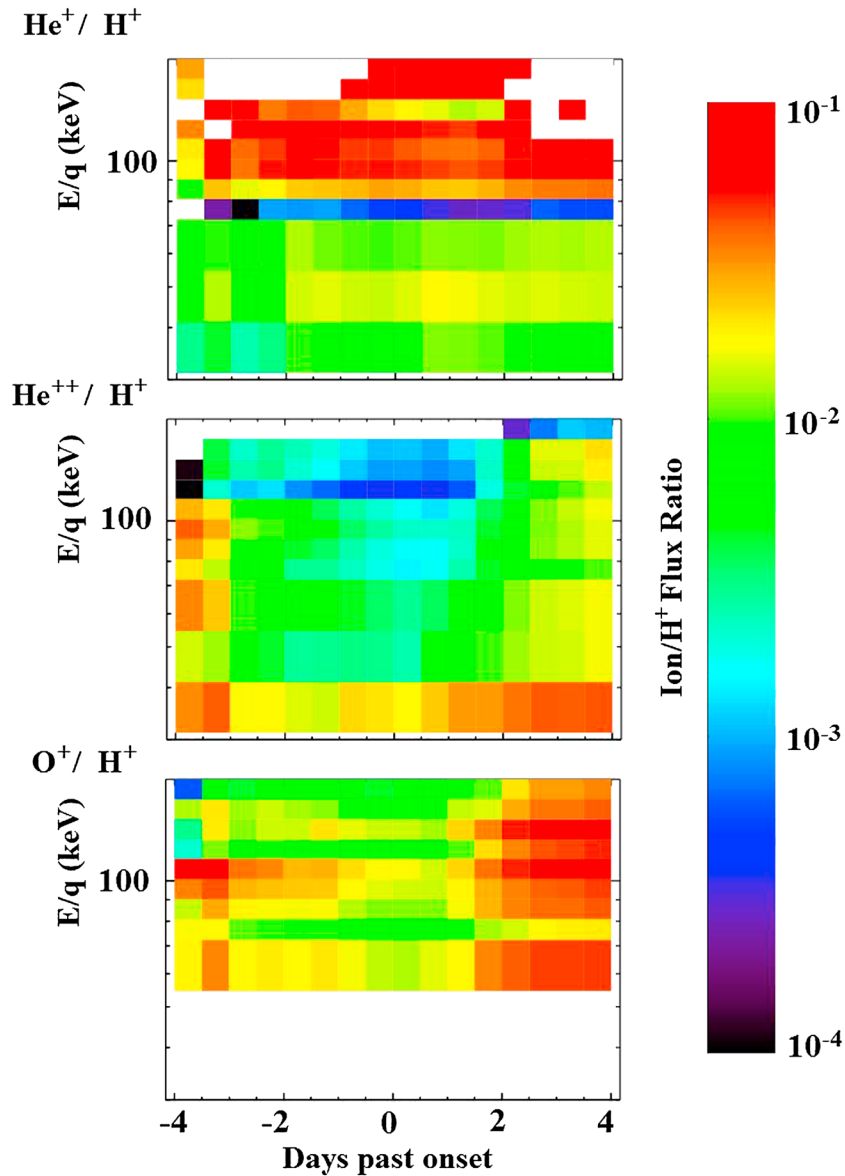


Figure 9. Superposed epoch analysis of five HSS events from 1991, showing E/q orbit-averaged heavy ion to H^+ flux ratios. Specifically, (top) He^+/H^+ , (middle) He^{++}/H^+ , and (bottom) O^+/H^+ are shown. The heavy ion content of the ring current shows a clear dropout out across zero, most clearly observed in O^+ and He^{++} .

after onset and is more rapid at lower energies: in He^{++} data, the flux surpasses its pre-onset value 20–30 h after onset in the energy range 31.2–41.2 keV but takes between approximately 50 and 80 h to surpass its predropout level at ~ 100 keV. All species show greater fluxes of particles in the days following than during the days prior to onset.

[25] Figure 8 contains graphs showing flux data in energy ranges 31.2–54.6 keV (blue) and 81.0–175.0 keV (red) for H^+ (top), He^+ (upper middle), He^{++} (lower middle), and O^+ (bottom). Error bars show the standard mean error within each time-bin, these are observed to become generally larger during the recovery of the dropout (following onset), indicating a large level of variance during this period. In all species, the reduction in flux commences prior to onset at both low and high energies. Between ~ -30 and -50 h, there exists an enhancement in O^+ and He^+ which is coupled with large standard error, indicating that one or more of the events

contained an influx of heavy ion material to the ring current at this time (investigation of included events confirms this). Recovery of ions begins immediately following onset for all species. Low-energy ions are observed to recover more rapidly than high-energy ions for H^+ , He^+ , and He^{++} . There is no low-energy data available for O^+ . The flux of He^{++} and O^+ following recovery is greater than the pre-onset flux, creating a weakly enhanced ring current that leads to a weak reduction in the average D_{ST} index as seen in Figure 5.

[26] Figure 9 contains a superposed epoch analysis of heavy ion to H^+ flux ratios in the energy range 31.2–175.0 keV, showing He^+/H^+ (top), He^{++}/H^+ (middle), and O^+/H^+ (bottom). Instrumental noise was clear in the data and was removed prior to ratio calculation in this figure. The color scale (right) indicates the magnitude of the ratio. It is clear that H^+ always exists in greater fluxes than He^+ , He^{++} , or O^+ by at least an order of magnitude. There is a clear dropout in He^{++}/H^+ and

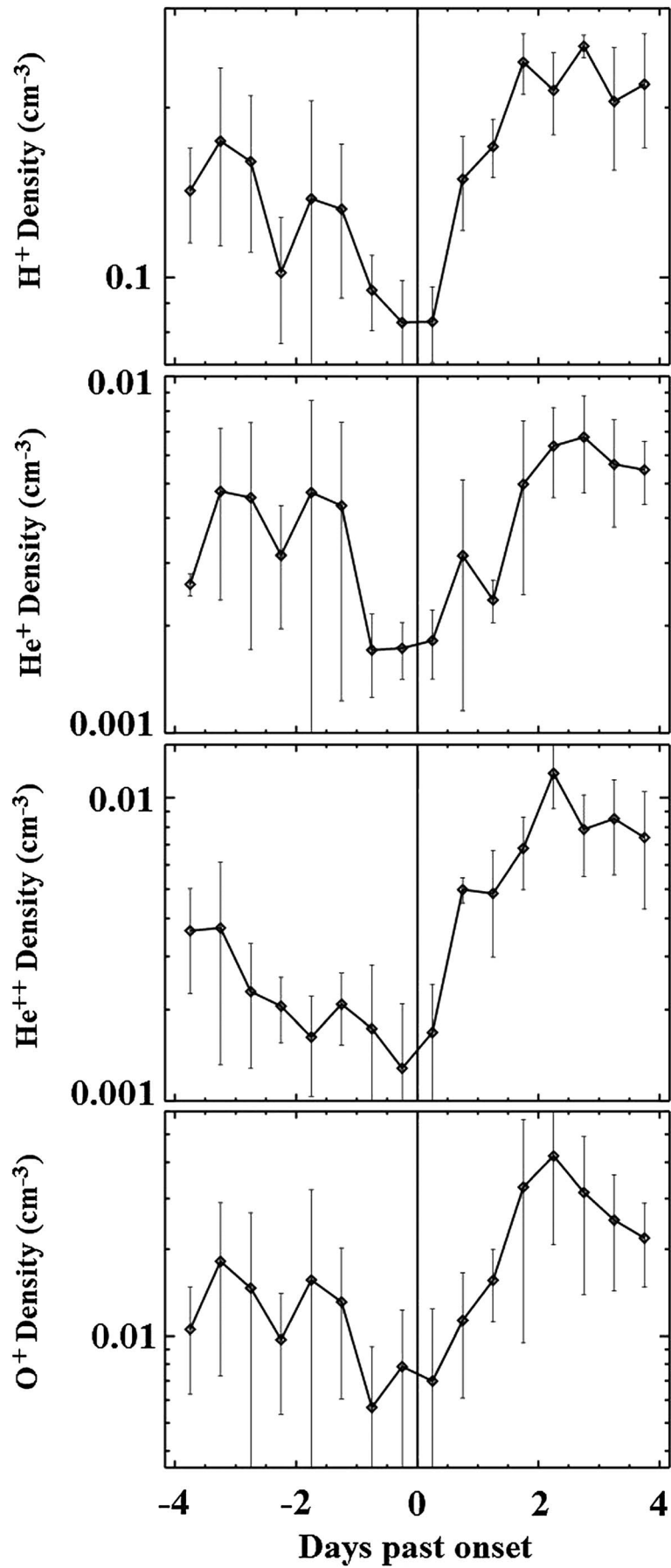


Figure 10

O^+/H^+ ratios with the minimum value being reached at onset. At this point, the ion ratios have dropped by approximately an order of magnitude; O^+/H^+ having decreased from $\sim 10^{-1}$ to $\sim 10^{-2}$, while He^{++}/H^+ having decreased from $\sim 10^{-2}$ to $\sim 10^{-3}$. Following onset He^{++}/H^+ and O^+/H^+ flux ratios begin to recover; after around 40 h, they have recovered to their pre-onset values. The post-onset maximum ratio values appear to be similar to the pre-onset maximum ratio values. Figure 9 indicates that the heavy-ion-to-proton ratio is relatively low during the dropout phase, and following onset, it becomes relatively high as heavy ions are introduced to the storm time ring current.

[27] Figure 10 contains the superposed epoch analysis of partial number density for all five events, showing H^+ (top), He^+ (upper middle), He^{++} (lower middle), and O^+ (bottom). Error bars on each plot show the standard error on the mean value of all events which contributed to a given bin. Within this figure, a partial number density dropout is observed to occur in all species with a minimum partial density found close to zero epoch. All species show evidence of a substantial partial density enhancement following zero epoch to partial density levels greater than those pre-onset. The recovery of ionic partial number density is rapid, with H^+ , He^{++} , and O^+ all exceeding their pre-onset densities ~ 24 h after onset and continuing to increase thereafter (during the period when solar wind speed is elevated). The relative increase in H^+ is small compared to that of the heavier species— H^+ ions exhibit an approximate doubling in partial number density compared to their pre-onset level. He^{++} recovery is particularly rapid, increasing to relatively large values almost immediately after onset. The increase in He^{++} partial number density relative to pre-onset values is almost an entire order of magnitude. O^+ increases to approximately four times its pre-onset value. Like H^+ , the He^+ ions do not show a relatively large increase in partial number density following the dropout phase but are clearly enhanced.

4. Discussion

[28] Taken together, the results presented above indicate the occurrence of a “dropout” in the ion flux/density at the onset of HSS-driven storms and the subsequent “recovery” during the period when the solar wind speed is elevated. The behavior of ions during HSS events provides clues regarding the processes involved in their observed dropout and recovery. Since the ions and electrons are likely coupled to some degree (for example, through ion-dependent wave-particle interactions), then the behavior of ions may also have a bearing on study of the well-known dropout and recovery of electrons. However, the nature of the analyses presented above (necessitated by the lack of continuous solar wind data and the limited lifetime of the CRRES mission) means it is difficult to draw strong conclusions without further observations and/or modeling work. Despite this, it is possible to draw some meaningful conclusions. The

solar wind data shown in Figure 5 closely resemble those expected during HSS events, and the 27 day periodicity of the partial number density dropout (and recovery) observed in Figure 6 further confirms the identity of the events in this study as CIRs/HSSs. The ion dropout thus appears to be similar in form and structure to the electron dropout. The recovery of ions begins very shortly after the dropout, and the resulting fluxes are clearly more intense than those before the dropout. In He^{++} , it is clear that low-energy particles recover more rapidly than high-energy particles (as is the case for the electron dropout), and hence our analysis indicates that ion energization is occurring at the same time as solar wind with elevated velocity impinges on the magnetosphere. A variety of wave processes have been implicated in electron energization in the outer radiation belt during these periods of fast solar wind [Mann *et al.*, 2002; Horne *et al.*, 2006; Elkington, 2006], and similar processes may serve to heat the ions.

[29] Figure 8 shows evidence of the energization of ions more clearly. For all species, ions in the lower energy range (31.2–54.6 keV) recover more rapidly than those in the higher energy range (81.0–175.0 keV). This “recovery” is thus consistent with initial return of a “seed population” of lower-energy ions which undergoes subsequent heating/energization, as has been suggested to be the case for electrons in the same region [Baker *et al.*, 1989]. In Figure 8, the minimum value of the dropout is reached within a few hours of storm onset; previous work has shown that the electron dropout reaches its minimum at approximately the same time [Borovsky and Denton, 2009a]. However, the relative energy-dependent drift paths followed by positively charged or negatively charged particles implies they will travel/orbit around the Earth and encounter regions with highly different waves at different times. The complexity inherent in studying the physics in this region limits our ability to interpret the results without other coincident observations. Modeling calculations could shed light on the range of possible energization processes which may be at work.

[30] In the heavy-ion-to-proton flux ratios of He^+/H^+ , He^{++}/H^+ , and O^+/H^+ shown in Figure 9, there is a clear decrease in He^{++}/H^+ and O^+/H^+ , indicating that He^{++} and O^+ are depleted more readily than H^+ during the dropout phase of the events. The minimum in each of these ratios is reached approximately at onset, with the respective value having fallen by around an order of magnitude. The heavy-ion-to-proton ratio is an important value with regard to EMIC wave activity, with varied relative concentrations of heavy ions leading to modifications in EMIC wave generation and propagation [Gomberoff and Neira, 1983; Kozyra *et al.*, 1984; Thorne *et al.*, 2006; Summers *et al.*, 2007]. The observed behavior of the ratios in Figure 9 may therefore provide some clues regarding the loss processes which contribute to both ion and electron dropouts during HSS events. While dense cold ions in plasmaspheric plumes have been implicated in electron loss, the ion flux and density at these higher energies are orders of magnitude

Figure 10. Superposed epoch analysis of partial number density for five HSS events during 1991, showing (top) H^+ , (upper middle) He^+ , (lower middle) He^{++} , and (bottom) O^+ . O^+ partial density had to be calculated above 54.6 keV due to a lack of data below that energy. Data are averaged using 12 h time bins, with error bars indicating the standard error on the mean value in each bin. Across zero epoch, there is a dropout in the partial number density of all species. Following zero, the partial number density increases to magnitudes greater than pre-onset.

lower, although the growth of EMIC waves with ion density is not linear with respect to energy [Kozyra *et al.*, 1984] or species. Of perhaps more interest is the effect of keV ions on the growth of equatorial magnetosonic wave instabilities and subsequent effects on electron acceleration [Thomsen *et al.*, 2011]. We plan to investigate this further in future work.

[31] The minimum values in partial number density for all species, shown in Figure 10, are reached close to storm onset, with the recovery beginning immediately afterward. The recovery is rapid, with number densities surpassing pre-dropout values within a day of onset. He⁺⁺ is the species which shows the clearest partial number density dropout, and the He⁺ recovery is especially rapid. The number density increases by around an order of magnitude from the minimum. A comparison between this plot and the He⁺⁺ flux spectrogram shown in Figure 7 shows that the initial rapid increase in flux, of around a factor of 5, is due to He⁺⁺ in low-energy bins. The slower increase in partial number density following the initial recovery is coincident with the expansion to higher energy in He⁺⁺ flux, which suggests energization of the particles at constant, or only slowly increasing, number density. The partial number density recovery of H⁺ is also rapid, but He⁺ and O⁺ are observed to increase less rapidly. Following recovery, the partial number density of all species is greater than that in pre-dropout—this is consistent with the idea of a “seed” population being energized during the period of elevated solar wind velocity.

5. Conclusions

[32] Average fluxes and partial number density of four ion species at energies 31.2–426.0 keV have been investigated during five HSS events in 1991. The main conclusions of this study are as follows:

[33] 1. A dropout occurs in all ionic species (O⁺, H⁺, He⁺, and He⁺⁺) during HSS storms. This dropout commences close to convection onset, and a minimum in the ion flux and the partial ion density are reached shortly afterward.

[34] 2. Recovery of ions follows the dropout, and after approximately 20–30 h, the average ion partial number density exceeds the pre-storm value.

[35] 3. The initial rapid recovery in partial number density is associated with an increase primarily in low-energy ions. As the partial number density recovers toward its maximum, the population as a whole shows evidence of energization.

[36] We strongly encourage modeling studies of energetic ion behavior during HSS events to shed light on physical mechanisms (e.g., transport, wave-particle interactions, atmospheric loss) at work during the ion dropout and subsequent recovery.

[37] **Acknowledgments.** This work was supported by STFC grant ST/G002401/1. The authors would like to thank the Space Physics Data Facility (SPDF) and National Space Science Data Center (NSSDC) for provision of the OMNI2 database and the World Data Centre for Geomagnetism in Kyoto for provision of the D_{ST} Index. MHD would like to thank Joe Borovsky (Space Science Institute) for helpful conversations. D. R. Forster would like to thank Richard Home and David Hartley for their useful comments

References

Baker, D. N., J. B. Blake, L. B. Callis, R. D. Belian, and T. E. Cayton (1989), Relativistic electrons near geostationary orbit: Evidence for internal magnetospheric acceleration, *Geophys. Res. Lett.*, *16*(6), 559–562, doi:10.1029/GL016i06p00559.

Borovsky, J. E., and T. E. Cayton (2011), Entropy mapping of the outer electron radiation belt between the magnetotail and geosynchronous orbit, *J. Geophys. Res.*, *116*, A06216, doi:10.1029/2011JA016470.

Borovsky, J. E., and M. H. Denton (2006), The differences between CME-driven storms and CIR-driven storms, *J. Geophys. Res.*, *111*, A07S08, doi:10.1029/2005JA011447.

Borovsky, J. E., and M. H. Denton (2009a), Relativistic electron dropouts and recovery: A superposed-epoch study of the magnetosphere and the solar wind, *J. Geophys. Res.*, *114*, A02201, doi:10.1029/2008JA013128.

Borovsky, J. E., and M. H. Denton (2009b), Electron loss rates from the outer electron radiation belt caused by the filling of the outer plasmasphere: The calm before the storm, *J. Geophys. Res.*, *114*, A11203, doi:10.1029/2009JA014063.

Borovsky, J. E., and J. T. Steinberg (2006), The “calm before the storm” in CIR/magnetospheric interactions: Occurrence statistics, solar wind statistics, and magnetospheric preconditioning, *J. Geophys. Res.*, *111*, A07S10, doi:10.1029/2005JA011397.

Cayton, T. E., R. D. Belian, S. P. Gary, T. A. Fritz, and D. N. Baker (1989), Energetic electron components at geosynchronous orbit, *Geophys. Res. Lett.*, *16*(2), 147–150, doi:10.1029/GL016i02p0147.

Ciliverd, M. A., T. D. G. Clark, A. J. Smith, and N. R. Thomson (1993), Observation of a decrease in mid-latitude whistler mode signal occurrence prior to geomagnetic storms, *J. Atmos. Terr. Phys.*, *55*(10), 1479–1485, doi:10.1016/0021-9169(93)90113-D.

Denton, M. H., and J. E. Borovsky (2008), Superposed epoch analysis of high-speed-stream effects at geosynchronous orbit: Hot plasma, cold plasma, and the solar wind, *J. Geophys. Res.*, *113*, A07216, doi:10.1029/2007JA012998.

Denton, M. H., and J. E. Borovsky (2009), The superdense plasma sheet in the magnetosphere during high-speed-stream-driven storms: Plasma transport timescales, *J. Atmos. Sol. Terr. Phys.*, *71*, 1045, doi:10.1029/2008.04.023.

Denton, M. H., and T. E. Cayton (2011), Density and temperature of energetic electrons in the Earth’s magnetotail derived from high-latitude GPS observations during the declining phase of the solar cycle, *Ann. Geophys.*, *29*, 1755–1763, doi:10.5194/angeo-29-1755-2011.

Denton, M. H., T. Ulich, and E. Turunen (2009a), Modification of midlatitude ionospheric parameters in the F2 layer by persistent solar wind streams, *Space Weather*, *7*, S04006, doi:10.1029/2008SW000443.

Denton, M. H., J. E. Borovsky, R. B. Home, R. L. McPherron, S. K. Morley, and B. T. Tsurutani (2009b), Introduction to special issue on high speed solar wind streams and geospace interactions, *J. Atmos. Sol. Terr. Phys.*, *71*, 1364–6826, doi:10.1016/j.jastp.2008.09.019.

Denton, M. H., J. E. Borovsky, and T. E. Cayton (2010), A density-temperature description of the outer electron radiation belt during geomagnetic storms, *J. Geophys. Res.*, *115*, A01208, doi:10.1029/2009JA014183.

Elkington, S. R. (2006), A review of ULF interactions with radiation belt electrons, *Geophys. Monogr. Ser.*, *169*, 177–193, doi:10.1029/169GM12.

Fraser, B. J., R. S. Grew, S. K. Morley, J. C. Green, H. J. Singer, T. M. Loto’aniu, and M. F. Thomsen (2010), Storm time observations of electromagnetic ion cyclotron waves at geosynchronous orbit: GOES results, *J. Geophys. Res.*, *115*, A05208, doi:10.1029/2009JA014516.

Gomberoff, L., and R. Neira (1983), Convective growth rate of ion cyclotron waves in a H/He+H+/He+O+ plasma, *J. Geophys. Res.*, *88*(A3), 2170–2174, doi:10.1029/JA088iA03p02170.

Green, J. C., T. G. Onsager, T. P. O’Brien, and D. N. Baker (2004), Testing loss mechanisms capable of rapidly depleting relativistic electron flux in the Earth’s outer radiation belt, *J. Geophys. Res.*, *109*, A12211, doi:10.1029/2004JA010579.

Home, R. B., and R. M. Thorne (1998), Potential waves for relativistic electron scattering and stochastic acceleration during magnetic storms, *Geophys. Res. Lett.*, *25*(15), 3011–3014, doi:10.1029/98GL01002.

Home, R. B., and R. M. Thorne (2000), Electron pitch angle diffusion by electrostatic electron cyclotron harmonic waves: The origin of pancake distributions, *J. Geophys. Res.*, *105*(A3), 5391–5402, doi:10.1029/1999JA900447.

Home, R. B., and R. M. Thorne (2003), Relativistic electron acceleration and precipitation during resonant interactions with whistler mode chorus, *Geophys. Res. Lett.*, *30*(10), 1527, doi:10.1029/2003GL016973.

Home, R. B., G. V. Wheeler, and H. S. C. K. Alleyne (2000), Proton and electron heating by radially propagating fast magnetosonic waves, *J. Geophys. Res.*, *105*(A12), 27,597–527,610, doi:10.1029/2000JA000018.

Home, R. B., N. P. Meredith, S. A. Glauert, D. Varotsou, D. Boscher, R. M. Thorne, Y. Y. Shprits, and R. R. Anderson (2006), Mechanisms for the acceleration of radiation belt electrons, *Geophys. Monogr. Ser.*, *167*, 151–173, doi:10.1029/167GM14.

Ilie, R., M. W. Liemohn, M. F. Thomsen, J. E. Borovsky, and J. Zhang (2008), Influence of epoch time selection on the results of superposed epoch analysis using ACE and MPA data, *J. Geophys. Res.*, *113*, A00A14, doi:10.1029/2008JA013241.

- Jordanova, V. K., H. Matsui, P. A. Puhl-Quinn, M. F. Thomsen, K. Mursula, and L. Holappa (2009), Ring current development during high speed streams, *J. Atmos. Sol. Terr. Phys.*, *71*(10-11), doi:10.1016/j.jastp.2008.09.043.
- Kim, H.-J., and A. A. Chan (1997), Fully adiabatic changes in storm time relativistic electron fluxes, *J. Geophys. Res.*, *102*(A10), 107, doi:10.1029/97JA01814.
- Kim, K. C., D.-Y. Lee, H.-J. Kim, E. S. Lee, and C. R. Choi (2010), Numerical estimates of drift loss and Dst effect for outer radiation belt relativistic electrons with arbitrary pitch angle, *J. Geophys. Res.*, *115*, A03208, doi:10.1029/2009JA014523.
- King, J. H., and N. Papitashvili (2005), Solar wind spatial scales in and comparisons of hourly Wind and ACE plasma and magnetic field data, *J. Geophys. Res.*, *110*, A02104, doi:10.1029/2004JA010649.
- Kozyra, J. U., T. E. Cravens, A. F. Nagy, E. G. Fontheim, and R. S. B. Ong (1984), Effects of energetic heavy ions on electromagnetic ion cyclotron wave generation in the plasmapause region, *J. Geophys. Res.*, *89*(A4), 2217–2233, doi:10.1029/JA089iA04p02217.
- Lam, M. M., R. B. Horne, N. P. Meredith, and S. A. Glauert (2007), Modeling the effects of radial diffusion and plasmaspheric hiss on outer radiation belt electrons, *Geophys. Res. Lett.*, *34*, L20112, doi:10.1029/2007GL031598.
- Lam, M. M., R. B. Horne, N. P. Meredith, and S. A. Glauert (2009), Radiation belt electron flux variability during three CIR-driven geomagnetic storms, *J. Atmos. Sol. Terr. Phys.*, *71*(10-11), 1145–1156, doi:10.1016/j.jastp.2008.06.007.
- Liemohn, M. W., A. J. Ridley, J. U. Kozyra, D. L. Gallagher, M. F. Thomsen, M. G. Henderson, M. H. Denton, P. C. Brandt, and J. Goldstein (2006), Analyzing electric field morphology through data model comparisons of the GEM IM/S assessment challenge events, *J. Geophys. Res.*, *111*, A11S11, doi:10.1029/2006JA011700.
- MacDonald, E. A., L. W. Blum, S. P. Gary, M. F. Thomsen, and M. H. Denton (2010), High-speed stream driven inferences of global wave distributions at geosynchronous orbit: Relevance to radiation-belt dynamics, *Proc. R. Soc. A*, *466*, 3351–3362, doi:10.1098/rspa.2010.0076.
- Mann, I. R., et al. (2002), Coordinated ground based and Cluster observations of large amplitude global magnetospheric oscillations during a fast solar wind speed interval, *Ann. Geophys.*, *20*, 405–426, doi:10.5194/angeo-20-405-2002.
- McPherron, R. L., D. N. Baker, and N. U. Crooker (2009), Role of the Russell-McPherron effect in the acceleration of relativistic electrons, *J. Atmos. Sol. Terr. Phys.*, *71*, 1032, doi:10.1026/j.jastp.2008.11.002.
- Meredith, N. P., R. B. Horne, R. H. A. Iles, R. M. Thorne, D. Heynderickx, and R. R. Anderson (2002), Outer zone relativistic electron acceleration associated with substorm-enhanced whistlermode chorus, *J. Geophys. Res.*, *107*(A7), 1144, doi:10.1029/2001JA900146.
- Meredith, N. P., R. M. Thorne, R. B. Horne, D. Summers, B. J. Fraser, and R. R. Anderson (2003), Statistical analysis of relativistic electron energies for cyclotron resonance with EMIC waves observed on CRRES, *J. Geophys. Res.*, *108*(A6), 1250, doi:10.1029/2002JA009700.
- Meredith, N. P., R. B. Horne, M. M. Lam, M. H. Denton, J. E. Borovsky, and J. C. Green (2011), Energetic electron precipitation during high-speed solar wind stream driven storms, *J. Geophys. Res.*, *116*, A05233, doi:10.1029/2010JA016293.
- Millan, R. M., and R. M. Thorne (2007), Review of radiation belt relativistic electron losses, *J. Atmos. Sol. Terr. Phys.*, *69*, 362–377, doi:10.1016/j.jastp.2006.06.019.
- Mlynczak, M. G., L. A. Hunt, J. U. Kozyra, and J. M. Russell (2010), Short term periodic features observed in the infrared cooling of the thermosphere and in solar and geomagnetic indexes from 2000 to 2009, *Proc. R. Soc. A*, *466*, 3409–3419, doi:10.1098/rspa.2010.0077.
- O'Brien, T. P., R. L. McPherron, D. Sornette, G. D. Reeves, R. H. W. Friedel, and H. J. Singer (2001), Which magnetic storms produce relativistic electrons at geosynchronous orbit, *J. Geophys. Res.*, *106*(A8), 15,533–15,544, doi:10.1029/2001JA000052.
- Pokhotelov, D. C., P. T. Jayachandran, N. Mitchell, and M. H. Denton (2010), High-latitude ionospheric response to co-rotating interaction region- and coronal mass ejection-driven geomagnetic storms revealed by GPS tomography and ionosondes, *Proc. R. Soc. A*, doi:10.1098/rspa.2010.0800.
- Posch, J. L., M. J. Engebretson, M. T. Murphy, M. H. Denton, M. R. Lessard, and R. B. Horne (2010), Probing the relationship between electromagnetic ion cyclotron waves and plasmaspheric plumes near geosynchronous orbit, *J. Geophys. Res.*, *115*, A11205, doi:10.1029/2010JA015446.
- Reeves, G. D., D. N. Baker, R. D. Belian, J. B. Blake, T. E. Cayton, J. F. Fennell, R. H. W. Friedel, M. M. Meier, R. S. Selesnick, and H. E. Spence (1998), The global response of relativistic radiation belt electrons to the January 1997 magnetic cloud, *Geophys. Res. Lett.*, *25*(17), 3265, doi:10.1029/98GL02509.
- Rodger, C. J., M. A. Raita, M. A. Clilverd, A. Seppälä, S. Dietrich, N. R. Thomsen, and T. Ulich (2008), Observations of relativistic electron precipitation from the radiation belts driven by EMIC waves, *Geophys. Res. Lett.*, *35*, L16106, doi:10.1029/2008GL034804.
- Sandanger, M. I., F. Soraas, M. Sorbo, K. Aarsnes, K. Oksavik, and D. S. Evans (2009), Relativistic electron losses related to EMIC waves during CIR and CME storms, *J. Atmos. Sol. Terr. Phys.*, *71*, 1126–1144, doi:10.1016/j.jastp.2008.07.006.
- Shprits, Y. Y., and R. M. Thorne (2004), Time dependent radial diffusion modeling of relativistic electrons with realistic loss rates, *Geophys. Res. Lett.*, *31*, L08805, doi:10.1029/2004GL019591.
- Shprits, Y. Y., R. M. Thorne, R. H. W. Friedel, G. D. Reeves, J. Fennell, D. N. Baker, and S. G. Kanekal (2006), Outward radial diffusion driven by losses at magnetopause, *J. Geophys. Res.*, *111*, A11214, doi:10.1029/2006JA011657.
- Summers, D., and R. M. Thorne (2003), Relativistic electron pitch-angle scattering by electromagnetic ion cyclotron waves during geomagnetic storms, *J. Geophys. Res.*, *108*(A4), 1143, doi:10.1029/2002JA009489.
- Summers, D., B. Ni, and N. P. Meredith (2007), Timescales for radiation belt electron acceleration and loss due to resonant wave-particle interactions: 2. Evaluation for VLF chorus, ELF hiss, and electromagnetic ion cyclotron waves, *J. Geophys. Res.*, *112*, A04207, doi:10.1029/2006JA11993.
- Thomsen, M. F. (2004), Why Kp is such a good measure of magnetospheric convection, *Space Weather*, *2*, S11004, doi:10.1029/2004SW000089.
- Thomsen, M. F., M. H. Denton, V. K. Jordanova, L. Chen, and R. M. Thorne (2011), Free energy to drive the magnetospheric instability at geosynchronous orbit, *J. Geophys. Res.*, *116*, A08220, doi:10.1029/2011JA016644.
- Thorne, R. M., R. B. Horne, V. K. Jordanova, J. Bortnik, and S. A. Glauert (2006), Interaction of EMIC waves with thermal plasma and radiation belt particles, *Geophys. Monogr. Ser.*, *169*, 213–223.
- Tsurutani, B. T., R. L. McPherron, W. D. Gonzalez, G. Lu, N. Gopalswamy, and F. L. Guatnieri (2006), Magnetic storms caused by corotating solar wind streams, *Geophys. Monogr. Ser.*, *167*, 1–18.
- Turunen, E., P. T. Verronen, A. Seppälä, C. J. Rodger, M. A. Clilverd, J. Tamminen, C.-F. Enell, and T. Ulich (2009), Impact of different energies of precipitating particles on NOx generation in the middle and upper atmosphere during geomagnetic storms, *J. Atmos. Sol. Terr. Phys.*, *71*, 1176–1189, doi:10.1016/j.jastp.2008.07.005.
- Ukhorskiy, A. Y., B. J. Anderson, P. C. Brandt, and N. A. Tsyganenko (2006), Storm time evolution of the outer radiation belt: Transport and losses, *J. Geophys. Res.*, *111*, A11S03, doi:10.1029/2006JA011690.
- Wilken, B., W. Weiss, D. Hall, M. Grande, F. Soraas, and J. F. Fennell (1992), Magnetospheric ion composition spectrometer onboard the CRRES spacecraft, *J. Spacecraft Rockets*, *29*(4), 585–591, doi:10.2514/3.25503.